Alignment-Based Optically Pumped Magnetometer Using a Buffer-Gas Cell

L.M. Rushton⊙,[*] L. Elson⊙, A. Meraki⊙, and K. Jensen⊙[†]

*School of Physics and Astronomy, University of Nottingham, University Park, Nottingham NG7 2RD,
United Kingdom*

Alignment-based optically pumped magnetometers (OPMs) are capable of measuring oscillating magnetic fields with high sensitivity in the $fT/\sqrt{Hz}$ range. Until now, alignment-based magnetometers have only used paraffin-coated vapour cells to extend the spin relaxation lifetimes of the alkali vapour. The drawback of these cells is that they are hand blown and are therefore time intensive, and somewhat unreliable, to produce. Buffer-gas cells, on the other hand, can be manufactured on a mass scale using microfabrication techniques. In this work we use hand-blown cells, but our methods also apply to microfabricated buffer-gas cells. We present the first demonstration of an alignment-based magnetometer using a buffer-gas vapour cell containing caesium (Cs) alkali vapour and nitrogen (N_2) buffer gas. The OPM is operated at $55\,^\circ$C and we achieve a $325\ fT/\sqrt{Hz}$ sensitivity to 10 kHz oscillating magnetic fields with an 800 Hz bandwidth. The alignment-based magnetometer uses a single low-power laser beam for optical pumping and probing and could potentially allow for more rapid commercialization of radio-frequency OPMs, due to the robustness of the one-beam geometry.

I. INTRODUCTION

Optically pumped magnetometers (OPMs) [1–4] based on spin-polarized atoms [e.g., alkali atoms such as caesium (Cs) or rubidium] can measure magnetic fields with high sensitivity in the $fT/\sqrt{Hz}$ range [5–9]. Current commercial OPMs [10–12] are operated close to zero magnetic field in the spin-exchange relaxation-free regime measuring one, two, or three components of the magnetic field, or in the Earth's field as scalar magnetometers measuring the total magnetic field amplitude. These OPMs use one or two beams of circularly polarized light generated from a single laser diode inside the OPM, making the sensors compact and robust. The circularly polarized light effectively generates spin orientation along the light propagation (i.e., the atomic spins point in a certain direction) that responds to magnetic fields and can be measured by detecting the transmitted light. When detecting oscillating magnetic fields in the kilohertz–megahertz frequency range, radio-frequency (rf) OPMs [13–22] must be used. One type of rf OPM using only a single laser beam is the alignment-based magnetometer (also called a "double

resonance alignment magnetometer" or an "rf OPM based on nonlinear magneto-optical rotation") [23–27], which uses linearly polarized light capable of effectively aligning the atoms in the direction perpendicular to its propagation. As a result, as the rf field affects such alignment being created, its presence can be sensed directly by measuring properties of the same beam.

High sensitivity optical magnetometry requires a long atomic spin-coherence time. This can be achieved using vapour cells coated on the inside with an antirelaxation coating (e.g., paraffin), such that the moving alkali atoms can bounce off the inner glass walls of the vapour cell many times without losing their spin coherence [28,29]. Alternatively, a long coherence time can be achieved by filling the vapour cell with buffer gas (e.g., N_2). Rapid collisions between the buffer-gas atoms and the alkali atoms make the alkali atoms diffuse slowly, which mitigates the effects of spin-destroying wall collisions. Alkali vapour cells for magnetometry are typically hand blown; however, buffer-gas cells for magnetometry can be produced on a mass scale using microfabrication techniques [30,31]. Such microfabrication techniques have not, as of yet, been compatible with antirelaxation coating.

So far, alignment-based optical magnetometry has been demonstrated using hand-blown, antirelaxation coated cells [23,24]. The presence of buffer gas leads to pressure broadening of the alkali vapour absorption spectrum, reducing the light-atom coupling and affecting the optical pumping preparing the aligned state. The buffer gas N_2 is also a quenching gas [32] that causes the alkali atoms not to

[*]lucasrushton@outlook.com

[†]kasper.jensen@nottingham.ac.uk

deexcite via spontaneous emission. Rapid collisional mixing in the excited state [32] also occurs in buffer-gas cells, but not in paraffin-coated cells. We show here that, despite these complexities, it is possible to realize an alignment-based magnetometer using a buffer-gas cell. We experimentally demonstrate an alignment-based magnetometer using a Cs alkali vapour and 65 Torr N_2 buffer-gas cell with a sensitivity of 325 fT/$\sqrt{\text{Hz}}$ to oscillating magnetic fields at 10 kHz. We also demonstrate an alignment-based magnetometer with a paraffin-coated cell placed in the same experimental setup to verify the methods and for comparison. Our results open up the possibility for miniaturization [20,33] and commercialization of rf OPMs, with potential impact in areas such as medical physics [34–36], remote sensing [33,37], and nondestructive testing [38,39].

II. ALIGNMENT-BASED OPTICAL MAGNETOMETRY

The theory underpinning the alignment-based magnetometer [2,17,24,25] will now be revised and discussed. Consider atoms with a $F = 1 \rightarrow F' = 0$ optical transition with ground-state sublevels $|F, m\rangle = \{|1, 1\rangle, |1, 0\rangle, |1, -1\rangle\}$ and an excited state $|F', m'\rangle = |0', 0'\rangle$, as shown in Fig. 1(a). A single laser beam is used for optical pumping and probing of the atoms. Assume that the light is linearly (π) polarized along the direction of a static magnetic field $B_0 \hat{\mathbf{z}}$. In this case, the atoms will be optically pumped into the $m = \pm 1$ sublevels with equal probability, creating a so-called "spin-aligned state." This is a dark state, such that with perfect optical pumping, the light will be fully transmitted through the atomic vapour. Now assume further that there is a transverse oscillating (rf) magnetic field that we would like to detect. That rf field will affect the optical pumping and thereby the transmitted light that can be detected by measuring its intensity or polarization.

The total Hamiltonian $\hat{H}$ that describes the system is given by

$$\hat{H} = \hat{H}_0 + \hat{H}_l + \hat{H}_B, \tag{1}$$

where $\hat{H}_0$, $\hat{H}_l$, and $\hat{H}_B$ are the unperturbed, light-atom interaction and magnetic field-atom interaction Hamiltonians, respectively. The unperturbed Hamiltonian $\hat{H}_0$ written in the overall basis $\{|1, 1\rangle \equiv |1\rangle, |1, 0\rangle \equiv |0\rangle, |1, -1\rangle \equiv |-1\rangle, |0', 0'\rangle \equiv |0'\rangle\}$ is

$$\hat{H}_0 = \begin{pmatrix} 0 & 0 & 0 & 0 \\ 0 & 0 & 0 & 0 \\ 0 & 0 & 0 & 0 \\ 0 & 0 & 0 & \hbar\omega_0 \end{pmatrix}, \tag{2}$$

where $\hbar$ is the reduced Planck constant, $\omega_0 = 2\pi c/\lambda$ is the optical transition frequency, λ its wavelength, and c the speed of light. The light-atom interaction is governed by

$$\hat{H}_l = -\mathbf{E} \cdot \hat{\mathbf{d}}, \tag{3}$$

where $\hat{\mathbf{d}}$ is the dipole operator and $\mathbf{E} = E_0 \cos(\omega t)\hat{\mathbf{z}}$ is the electric field of the light. The light-atom interaction Hamiltonian $\hat{H}_l$ is

$$\hat{H}_l = \hbar\Omega_R \cos\omega t \begin{pmatrix} 0 & 0 & 0 & 0 \\ 0 & 0 & 0 & -1 \\ 0 & 0 & 0 & 0 \\ 0 & -1 & 0 & 0 \end{pmatrix}, \tag{4}$$

where $\Omega_R = \langle 1||d||0'\rangle E_0/(\sqrt{3}\hbar)$ is the Rabi frequency and $\langle 1||d||0'\rangle$ is the transition dipole matrix element. Assuming that $B_x = B_{\text{rf}} \cos\omega_{\text{rf}}t$, $B_y = 0$, and $B_z = B_0$, the magnetic field-atom interaction is given by

$$\hat{H}_B = -\hat{\boldsymbol{\mu}} \cdot \mathbf{B} = \frac{g_F \mu_B}{\hbar}(\hat{F}_x B_x + \hat{F}_z B_z) = g_F \mu_B \begin{pmatrix} B_0 & B_{\text{rf}} \cos\omega_{\text{rf}}t/\sqrt{2} & 0 & 0 \\ B_{\text{rf}} \cos\omega_{\text{rf}}t/\sqrt{2} & 0 & B_{\text{rf}} \cos\omega_{\text{rf}}t/\sqrt{2} & 0 \\ 0 & B_{\text{rf}} \cos\omega_{\text{rf}}t/\sqrt{2} & -B_0 & 0 \\ 0 & 0 & 0 & 0 \end{pmatrix}. \tag{5}$$

Here $\hat{\boldsymbol{\mu}} = g_F \mu_B(\hat{F}_x \hat{\mathbf{x}} + \hat{F}_y \hat{\mathbf{y}} + \hat{F}_z \hat{\mathbf{z}})/\hbar$ is the Cs atom's magnetic dipole operator, g_F is the hyperfine Lande g factor [40], and μ_B is the Bohr magneton. Defining the Larmor frequency $\Omega_L = g_F \mu_B B_0/\hbar$ and letting the strength of the rf field be represented by $\Omega_{\text{rf}} = g_F \mu_B B_{\text{rf}}/\hbar$, the total Hamiltonian $\hat{H} = \hat{H}_0 + \hat{H}_B + \hat{H}_l$ is

$$\hat{H} = \hbar \begin{pmatrix} \Omega_L & \Omega_{\text{rf}} \cos\omega_{\text{rf}}t/\sqrt{2} & 0 & 0 \\ \Omega_{\text{rf}} \cos\omega_{\text{rf}}t/\sqrt{2} & 0 & \Omega_{\text{rf}} \cos\omega_{\text{rf}}t/\sqrt{2} & -\Omega_R \cos\omega t/\sqrt{3} \\ 0 & \Omega_{\text{rf}} \cos\omega_{\text{rf}}t/\sqrt{2} & -\Omega_L & 0 \\ 0 & -\Omega_R \cos\omega t/\sqrt{3} & 0 & \omega_0 \end{pmatrix}. \tag{6}$$
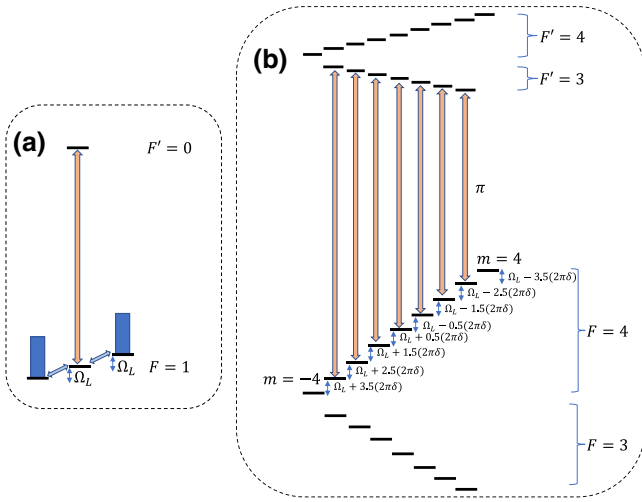
FIG. 1. (a) Energy level diagram with a $F = 1$ ground state and $F' = 0$ excited state. The neighboring ground-state sublevels are each split by the Larmor frequency Ω_L. Linearly polarized (π) light drives transitions between $m = 0$ and $m' = 0$. (b) D1 line of Cs with $F = 3, 4$ ground states and $F' = 3, 4$ excited states. Linearly polarized (π) light drives transitions between $F = 4$ and $F' = 3$. Small corrections (δ) for the nonlinear Zeeman splitting are shown.

Going to a rotating frame at the optical frequency ω, followed by going to another rotating frame at the rf frequency ω_{rf}, then neglecting the fast oscillating terms using the rotating-wave approximation and setting $\Delta = \omega - \omega_0$, $\Delta_{rf} = \omega_{rf} - \Omega_L$, Hamiltonian $\hat{\tilde{H}}$ in the rotating frame is

$$\hat{\tilde{H}} = \hbar \begin{pmatrix} -\Delta_{rf} & \Omega_{rf}/2\sqrt{2} & 0 & 0 \\ \Omega_{rf}/2\sqrt{2} & 0 & \Omega_{rf}/2\sqrt{2} & -\Omega_R/2\sqrt{3} \\ 0 & \Omega_{rf}/2\sqrt{2} & \Delta_{rf} & 0 \\ 0 & -\Omega_R/2\sqrt{3} & 0 & -\Delta \end{pmatrix}.$$

$$(7)$$

Next the relaxation $\hat{\Gamma}$ and repopulation $\hat{\Lambda}$ matrices must be taken into account and are given by

$$\hat{\Gamma} = \begin{pmatrix} \gamma & 0 & 0 & 0 \\ 0 & \gamma & 0 & 0 \\ 0 & 0 & \gamma & 0 \\ 0 & 0 & 0 & \gamma + \Gamma \end{pmatrix}, \quad (8)$$

$$\hat{\Lambda} = \begin{pmatrix} (\gamma + \Gamma\rho_{0',0'})/3 & 0 & 0 & 0 \\ 0 & (\gamma + \Gamma\rho_{0',0'})/3 & 0 & 0 \\ 0 & 0 & (\gamma + \Gamma\rho_{0',0'})/3 & 0 \\ 0 & 0 & 0 & 0 \end{pmatrix}.$$

$$(9)$$

The atoms in the excited state decay to ground-state sublevels at a rate Γ and are assumed to repopulate the three ground-state sublevels in equal proportion $\Gamma\rho_{0',0'}/3$,

where $\rho_{0',0'}$ is the population of the excited state. For a paraffin-coated cell, the excited atoms decay via spontaneous emission [at the rate 2π (4.56 MHz) [40] for Cs atoms in the first excited state]. For a buffer-gas cell, the excited atoms mainly decay via quenching, as discussed in the next section. Note that the model above only includes one excited state and therefore does not describe collisional mixing (between multiple excited states). The atoms also have a spin coherence (or transverse relaxation) time $T_2 = 1/\gamma$. In a buffer-gas cell, the alkali atoms diffuse slowly due to collisions with the buffer gas, increasing T_2. The spins relax when the alkali atoms hit the glass walls due to electron randomization collisions or via spin-exchange or spin-destruction collisions between two alkali atoms [1,23,41]. In a paraffin-coated cell the alkali atoms can bounce off the walls thousands of times before spin relaxation occurs [28]. Power broadening due to laser light also reduces T_2.

The Liouville equation for the density matrix $\hat{\tilde{\rho}}$ in the rotating frame is given by

$$i\hbar \frac{\partial \hat{\tilde{\rho}}}{\partial t} = [\hat{\tilde{H}}, \hat{\tilde{\rho}}] - i\hbar\frac{1}{2}(\hat{\Gamma}\hat{\tilde{\rho}} + \hat{\tilde{\rho}}\hat{\Gamma}) + i\hbar\hat{\Lambda}. \quad (10)$$

In the steady state $d\hat{\tilde{\rho}}/dt = 0$ and the right-hand side of the equation can be solved to determine $\hat{\tilde{\rho}}$ in the rotating frame. The density matrix is returned to the lab frame $\hat{\rho}$ by using a transformation matrix. The polarization $\mathbf{P} = n\text{Tr}(\hat{\rho}\hat{\mathbf{d}})$ of the atomic vapour can then be calculated, where n is the alkali atom number density. The formalism in Ref. [2] allows for the in-phase and out-of-phase rotations of a linearly polarized beam to be extracted [24,25]. The expressions for the in-phase $\partial\phi^{in}/\partial l$ and quadrature $\partial\phi^{out}/\partial l$ values are [24]

$$\frac{\partial\phi^{in}}{\partial l} = \frac{n\Delta_{rf}\lambda^2\Omega_{rf}(2\gamma^2 + 8\Delta_{rf}^2 - \Omega_{rf}^2)\Omega_R^2}{36\pi\Gamma\gamma(\gamma^2 + 4\Delta_{rf}^2 + \Omega_{rf}^2)[4(\gamma^2 + \Delta_{rf}^2) + \Omega_{rf}^2]}$$

$$\approx \frac{n\lambda^2}{72\pi}\frac{\Omega_R^2}{\Gamma}\Omega_{rf}\frac{\Delta_{rf}/\gamma}{\Delta_{rf}^2 + \gamma^2} \quad \text{for } \Omega_{rf}^2 \ll \gamma^2, \quad (11)$$

$$\frac{\partial\phi^{out}}{\partial l} = \frac{n\lambda^2\Omega_{rf}(4\gamma^2 + 16\Delta_{rf}^2 + \Omega_{rf}^2)\Omega_R^2}{72\pi\Gamma\gamma(\gamma^2 + 4\Delta_{rf}^2 + \Omega_{rf}^2)[4(\gamma^2 + \Delta_{rf}^2) + \Omega_{rf}^2]}$$

$$\approx \frac{n\lambda^2}{72\pi}\frac{\Omega_R^2}{\Gamma}\Omega_{rf}\frac{1}{\Delta_{rf}^2 + \gamma^2} \quad \text{for } \Omega_{rf}^2 \ll \gamma^2, \quad (12)$$

where l is the length of the vapour cell. In the limit when $\Omega_{rf}^2 \ll \gamma^2$, as is the case throughout this paper, $\partial\phi^{in}/\partial l$ and $\partial\phi^{out}/\partial l$ are proportional to the rf magnetic field amplitude $B_{rf} \propto \Omega_{rf}$ and have dispersive and absorptive Lorentzian lineshapes, respectively, when varying the rf detuning Δ_{rf}. The light polarization rotation is measured using a balanced photodetector and lock-in detection (at

the rf frequency), yielding the lock-in outputs that can be written as

$$X \propto \frac{\partial \phi^{\text{out}}}{\partial l} \propto B_{\text{rf}} \frac{1}{(\omega_{\text{rf}} - \Omega_L)^2 + \gamma^2}, \tag{13}$$

$$Y \propto \frac{\partial \phi^{\text{in}}}{\partial l} \propto B_{\text{rf}} \frac{(\omega_{\text{rf}} - \Omega_L)/\gamma}{(\omega_{\text{rf}} - \Omega_L)^2 + \gamma^2}, \tag{14}$$

$$R = \sqrt{X^2 + Y^2} = |X + iY| \propto B_{\text{rf}} \left| \frac{1 + i(\omega_{\text{rf}} - \Omega_L)/\gamma}{(\omega_{\text{rf}} - \Omega_L)^2 + \gamma^2} \right|. \tag{15}$$

III. CAESIUM

A. Optical pumping in a paraffin-coated cell

A caesium (Cs) atom [40] has two ground states with hyperfine quantum numbers $F = 3$ and $F = 4$ separated by the hyperfine splitting $\nu_{\text{hf}} = 9.192$ GHz. The first excited states have $F' = 3$ and $F' = 4$ with a hyperfine splitting of 1.2 GHz. The optical transition of interest for this experiment is the Cs D1 $F = 4 \rightarrow F' = 3$ transition using z-linearly polarized light [see Fig. 1(b)] with a wavelength around 895 nm. The optical pumping can be understood by determining the populations of the 16 magnetic sublevels of the Cs ground state using rate equations [42]. We first consider a paraffin-coated cell, where the decay from the excited state is by spontaneous emission. An example of the rate of change of the population of the magnetic sublevel $F = 4, m = 3$, $dp_{F=4,m=3}/dt$, i.e., the diagonal element of the density matrix, is

$$\frac{dp_{4,3}}{dt} = R_p(-p_{4,3}c_{4,3\leftrightarrow3',3'} + p_{4,2}c_{4,2\leftrightarrow3',2'}c_{4,3\leftrightarrow3',2'} + p_{4,3}c_{4,3\leftrightarrow3',3'}c_{4,3\leftrightarrow3',3'}) - \Gamma_1 p_{4,3} + \Gamma_1/16, \tag{16}$$

where R_p is the optical pumping rate, $p_{4,3} = p_{4,3}(t)$ is the population of the magnetic sublevel at time t, and $c_{4,2\leftrightarrow3',2'}$ is the Clebsch-Gordon coefficient squared [40] for the π transition from $F = 4, m = 2 \leftrightarrow F' = 3, m' = 2$, for example. The longitudinal relaxation rate Γ_1 is not measured experimentally in this work but is typically much smaller than the transverse relaxation rate γ [43]. The negative terms in Eq. (16) depopulate the magnetic sublevel and the positive terms repopulate the sublevel. The populations of the 16 magnetic sublevels in the $F = 3$ and $F = 4$ ground states in the steady state $(dp/dt = 0)$ are determined numerically and we plot these in Fig. 2(a). We see that the atoms in the $F = 4$ sublevels are symmetrically distributed with most atoms in the $m = \pm4$ sublevels, corresponding to a spin-aligned state. Note that many atoms are "lost" to the other ground state $F = 3$. These atoms are not probed as they are 9.192 GHz detuned from the light.

B. Optical pumping in a buffer-gas cell

If a buffer gas such as 65 Torr of N_2 is present in a Cs vapour cell without any paraffin coating then the Cs atoms will mostly decay via quenching rather than via spontaneous emission [32,44], as will now be shown. The many vibrational and rotational states of the quenching gas molecule, in this case N_2, mean that, when a Cs atom in the excited state collides with a N_2 molecule, the Cs atom can deexcite without the emission of a photon, instead transferring its energy to the many vibrational and rotational modes of the N_2 molecule. The quenching rate R_Q is given by

$$R_Q = n_Q \sigma_Q v_{\text{Cs},N_2}, \tag{17}$$

where $n_Q = P/(k_B T) = 1.91 \times 10^{24}$ m^{-3} is the number density of N_2 molecules at $T \sim 55\,^{\circ}$C, P is the pressure, k_B is the Boltzmann constant, $\sigma_Q = 5.5 \times 10^{-19}$ m^2 [32] is the quenching gas cross section for Cs and N_2 (at 100 $^{\circ}$C), and $v_{\text{Cs},N_2} = \sqrt{8k_B T/\pi M} = 548$ m/s is the relative velocity between a Cs atom and N_2 molecule. The mass $M = 3.84 \times 10^{-26}$ kg is the effective mass of a Cs atom and N_2 molecule, given by $M = m_{\text{Cs}} m_{N_2}/(m_{\text{Cs}} + m_{N_2})$. The quenching factor Q helps determine the dominant decay mechanism, whether by spontaneous emission $(Q = 1)$ or by quenching $(Q = 0)$, and is given by [32]

$$Q = \frac{1}{1 + R_Q \tau_{\text{nat}}}. \tag{18}$$

Calculating $R_Q = 5.9 \times 10^8$ s^{-1} from the parameters stated above for Cs and 65 Torr N_2 and taking the natural lifetime of the D1 excited state to be $\tau_{\text{nat}} = 35$ ns [40], then $Q = 0.05$. This means that, for the 65 Torr N_2 buffer-gas cell used in our experiments, the dominant deexcitation mechanism from the excited state is quenching. During quenching, the decay probabilities to the ground states are not governed by the Clebsch-Gordon coefficients. Instead the atoms decay with equal probability (1/16) to any of the $F = 3$ and $F = 4$ ground-state magnetic sublevels. Crucially, though, the $F = 4, m = \pm4$ states will still be dark states in the presence of N_2, a quenching gas. An example of a rate equation for the population $dp_{4,3}/dt$ of the $F = 4, m = 3$ magnetic sublevel is given by

$$\frac{dp_{4,3}}{dt} = R_p \Bigg(-p_{4,3}c_{4,3\leftrightarrow3',3'}$$
$$+ \frac{1}{16}[p_{4,3}c_{4,3\leftrightarrow3',3'} + p_{4,2}c_{4,2\leftrightarrow3',2'} + p_{4,1}c_{4,1\leftrightarrow3',1'}$$
$$+ p_{4,0}c_{4,0\leftrightarrow3',0'} + p_{4,-1}c_{4,-1\leftrightarrow3',-1'}$$
$$+ p_{4,-2}c_{4,-2\leftrightarrow3',-2'} + p_{4,-3}c_{4,-3\leftrightarrow3',-3'}] \Bigg)$$
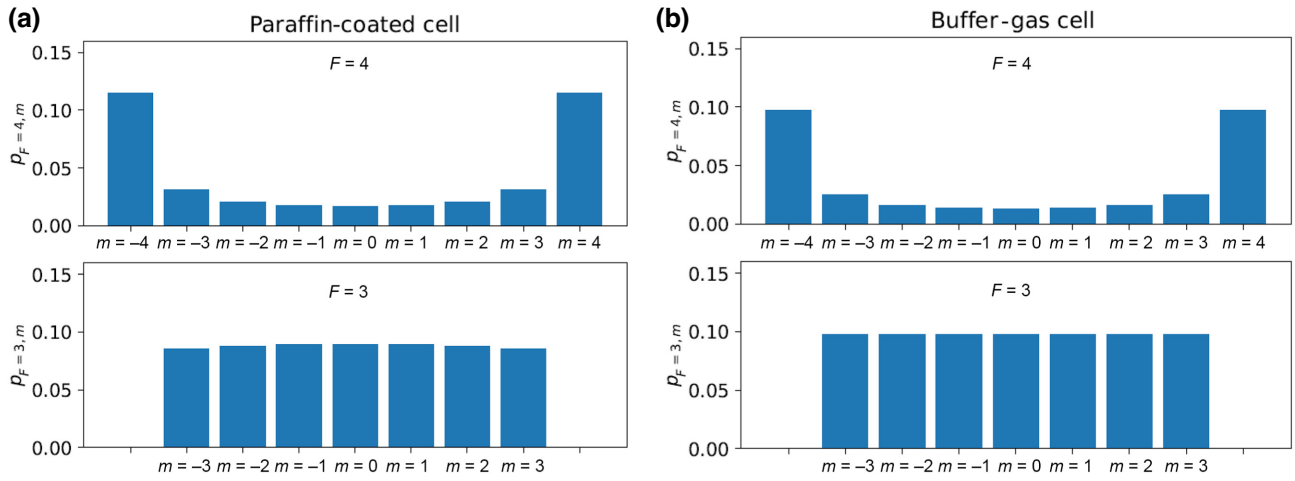$$- \Gamma_1 p_{4,3} + \frac{\Gamma_1}{16}. \tag{19}$$

FIG. 2.   Optical pumping from $F = 4 \rightarrow F' = 3$ with π-polarized light. The populations of the $F = 3$ and $F = 4$ ground-state magnetic sublevels in the steady state are plotted, with a longitudinal relaxation rate $\Gamma_1 = R_p/20$ for (a) a paraffin-coated cell where the dominant deexcitation mechanism from the excited state is spontaneous emission, and (b) a buffer-gas cell where the dominant deexcitation mechanism is quenching.

The 16 rate equations are solved in the steady state and an illustrative example of optical pumping with a buffer gas is shown in Fig. 2(b). We see that the distribution of atoms in the ground-state sublevels is similar for both buffer-gas and paraffin-coated vapour cells. It is assumed that $Q = 0$, which is a safe assumption to make for the 65 Torr N_2 buffer-gas cell in this paper. In the above we assumed that the excited states $F' = 3$ and $F' = 4$ are resolved such that the light is only resonant with the $F = 4 \rightarrow F' = 3$ transition. We note, however, that the $F' = 4$ excited state would need to be incorporated into the rate equations if the buffer-gas pressure becomes significantly larger, as discussed in Sec. V.

C. Nonlinear Zeeman splitting

A Cs atom in the $F = 4$ ground state has $2F + 1 = 9$ sublevels $|F, m\rangle$ that, when placed in a small magnetic field B_0, have the energy $E(m) = mh\nu_L$ due to the linear Zeeman effect. Here ν_L is the Larmor frequency in hertz. That is to say, the splittings between neighboring sublevels are all equal to the Larmor frequency $\Delta\nu_{m,m-1} \equiv (E(m) - E(m - 1))/h = \nu_L$. In this case, a single magnetic resonance will be observed when sweeping the rf frequency ν_{rf} (in hertz) across the Larmor frequency ν_L and measuring the polarization rotation of the transmitted light [see Eqs. (13), (14), and (15)]. However, at larger magnetic fields, the splittings between sublevels are slightly different due to the nonlinear Zeeman effect. We calculate [40,43,45]

$$\Delta\nu_{m,m-1} = \nu_L - \delta\left(m - \frac{1}{2}\right), \qquad (20)$$

where the nonlinear Zeeman splitting (in hertz) is

$$\delta = \frac{2\nu_L^2}{\nu_{hf}}, \qquad (21)$$

as illustrated in Fig. 1(b). In particular, the difference in transition frequencies between $\Delta\nu_{4,3}$ and $\Delta\nu_{-3,-4}$ is

$$|\Delta\nu_{4,3} - \Delta\nu_{-3,-4}| = 7\delta. \qquad (22)$$

In other words, at larger magnetic fields a total of eight magnetic resonances should be observed when sweeping the rf field across the Larmor frequency with the outermost resonances split by 7δ.

IV. PARAFFIN-COATED CELL

A schematic of the experimental setup is shown in Fig. 3(a). A diode laser system outputs light resonant with the $F = 4 \rightarrow F' = 3$ Cs D1 transition (895 nm). The light is passed through an optical fiber and is collimated at its output. The linearly polarized light with an electric field amplitude $E_0\hat{z}$ then passes through a cubic $(5 \text{ mm})^3$ hand-blown paraffin-coated vapour cell [see Fig. 3(b)]. The vapour cell is kept at room temperature (about 18.5 °C) and placed inside a magnetic shield (Twinleaf MS-1). Static $B_0\hat{z}$ and oscillating $B_{rf}\cos(2\pi\nu_{rf}t)\hat{x}$ magnetic fields can be applied using coils inside the magnetic shield. Here ν_{rf} is the rf frequency in hertz, while $\omega_{rf} = 2\pi\nu_{rf}$ is the rf frequency in rad/s. Polarimetry is then performed using a half-wave plate, a polarizing beam splitter, and a balanced photodetector (Thorlabs PDB210A/M) to detect the polarization rotation of the transmitted light. The resultant photodetector voltage is demodulated at the rf frequency ν_{rf} using a lock-in amplifier [Stanford Research Systems
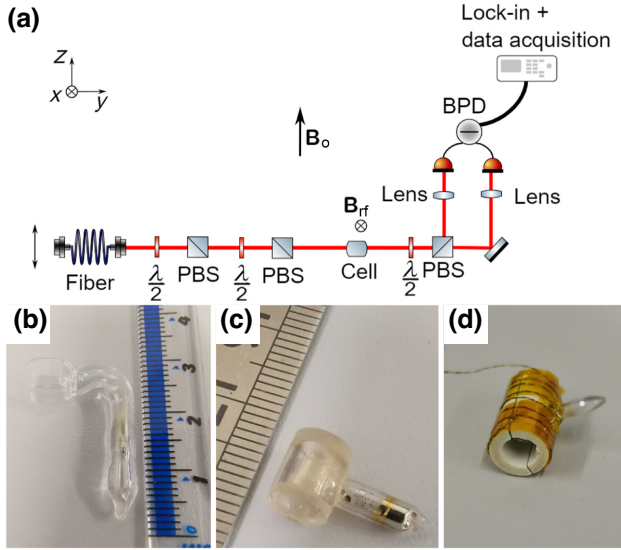
FIG. 3. (a) Schematic of an alignment-based magnetometer. The laser light propagates along the y direction and is z polarized. Components include half-wave plates ($\lambda/2$), polarizing beam splitters (PBSs), a vapour cell (Cell), and a balanced photodetector (BPD). Static $\mathbf{B}_0 = B_0\hat{\mathbf{z}}$ and oscillating magnetic fields $\mathbf{B}_{\mathrm{rf}}(t) = B_{\mathrm{rf}}(t)\hat{\mathbf{x}}$ are applied at the position of the vapour cell. The first half-wave plate and PBS after the fiber output are used to minimize the effects of polarization fluctuations due to, for example, temperature fluctuations. The second half-wave plate and PBS are used to vary the light power passing through the vapour cell. (b) Photo of the paraffin-coated cell. (c) Photo of the buffer-gas cell. (d) Photo of the buffer-gas cell surrounded by a Shapal ceramic cylinder, heating wires, and Kapton tape.
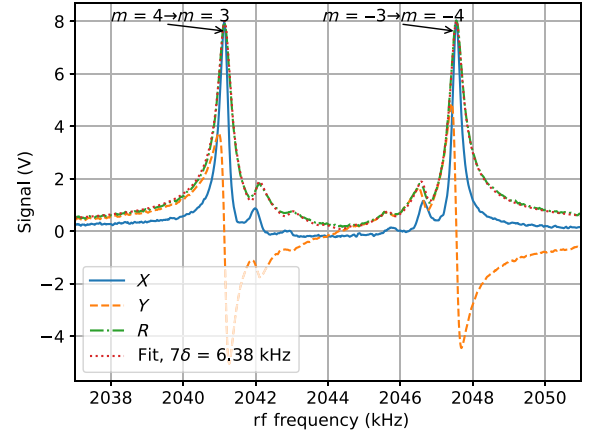

FIG. 4. Nonlinear Zeeman splitting of the magnetic resonances using a paraffin-coated cell. The magnitude R is fitted to Eq. (23). The fit is included as a dotted line. The magnetic resonances for $m = 4 \to m = 3$ and $m = -3 \to m = -4$, with different Larmor frequencies, are indicated.

(SRS) SR830] such that in-phase X and out-of-phase Y signals are obtained.

The optical pumping of an aligned state can be experimentally verified by exploiting the nonlinear Zeeman effect. These measurements are done at a relatively large static magnetic field ($B_0 = 5.84$ G) corresponding to a Larmor frequency close to 2 MHz. When the rf frequency is swept over the range 2.037–2.051 MHz, we observe a magnetic resonance spectrum with several peaks (see Fig. 4). The two largest peaks correspond to the transitions $m = 4 \to m = 3$ and $m = -3 \to m = -4$ with transition frequencies $\Delta\nu_{4,3}$ and $\Delta\nu_{-3,-4}$, respectively. The difference in transition frequencies $|\Delta\nu_{4,3} - \Delta\nu_{-3,-4}|$ is experimentally found to be 6.38(0.02) kHz, agreeing with the value $7\delta = 6.37$ kHz calculated from Eqs. (21) and (22), confirming that we are observing the nonlinear Zeeman splitting. This difference in transition frequencies is extracted by fitting the data of R in Fig. 4 to the function [43]

$$R = \left| \sum_{m=-3}^{4} \frac{A_{m,m-1}[1 + i(\nu_{\mathrm{rf}} - \nu_{m,m-1})/\tilde{\gamma}]}{(\nu_{\mathrm{rf}} - \nu_{m,m-1})^2 + \tilde{\gamma}^2} \right|, \quad (23)$$

which is a sum of eight magnetic resonances with resonance frequencies $\nu_{m,m-1} = \nu_L - \delta(m - 1/2)$ and half width at half maximum $\tilde{\gamma} = 1/(2\pi T_2)$ (in hertz), as seen by comparison with Eq. (15) and illustrated in Fig. 1. The data are fitted with seven free parameters: four amplitudes $A_{4,3}$, $A_{3,2}$, $A_{2,1}$, $A_{1,0}$ (as the magnetic resonance spectrum is symmetric such that $A_{0,-1} = A_{1,0}$, $A_{-1,-2} = A_{2,1}$, $A_{-2,-3} = A_{3,2}$, $A_{-3,-4} = A_{4,3}$), the Larmor frequency ν_L, the nonlinear Zeeman splitting δ, and the width $\tilde{\gamma}$.

In total, the spectrum has eight peaks, although the middle two are hardly visible in Fig. 4 due to their smaller height. The height of the individual peaks corresponding to $A_{m,m-1}/\tilde{\gamma}^2$ in Eq. (23) are proportional to the difference in populations of neighboring magnetic sublevels [43]. This is why there are eight peaks in the nonlinear Zeeman splitting, but nine populations in Fig. 2. As the outermost peaks are largest and have equal height, we conclude that an aligned state is created in the $F = 4$ ground state, with the majority of the atoms pumped into the $F = 4, m = \pm 4$ states. The optical pumping is not perfect as some of the atoms are pumped into the other magnetic sublevels. This is due to the nonzero longitudinal relaxation rate Γ_1.

We now proceed with characterizing the magnetic field sensitivity of the paraffin-coated vapour cell. These measurements are carried out at a smaller static magnetic field B_0 corresponding to a Larmor frequency of around 10 kHz. A 10 µW light power beam passes through the cell and a 4.22 nT$_{\mathrm{rms}}$ (20 mV$_{\mathrm{rms}}$) oscillating magnetic field is applied. A magnetic resonance signal is shown in Fig. 5(a), where the rf frequency is swept between 9 and 11.5 kHz and $\nu_L = 10.25$ kHz. From this, the peak of the resonance signal is extracted and divided by the applied oscillating magnetic field to give a conversion between the lock-in amplifier readout and the corresponding rf field amplitude
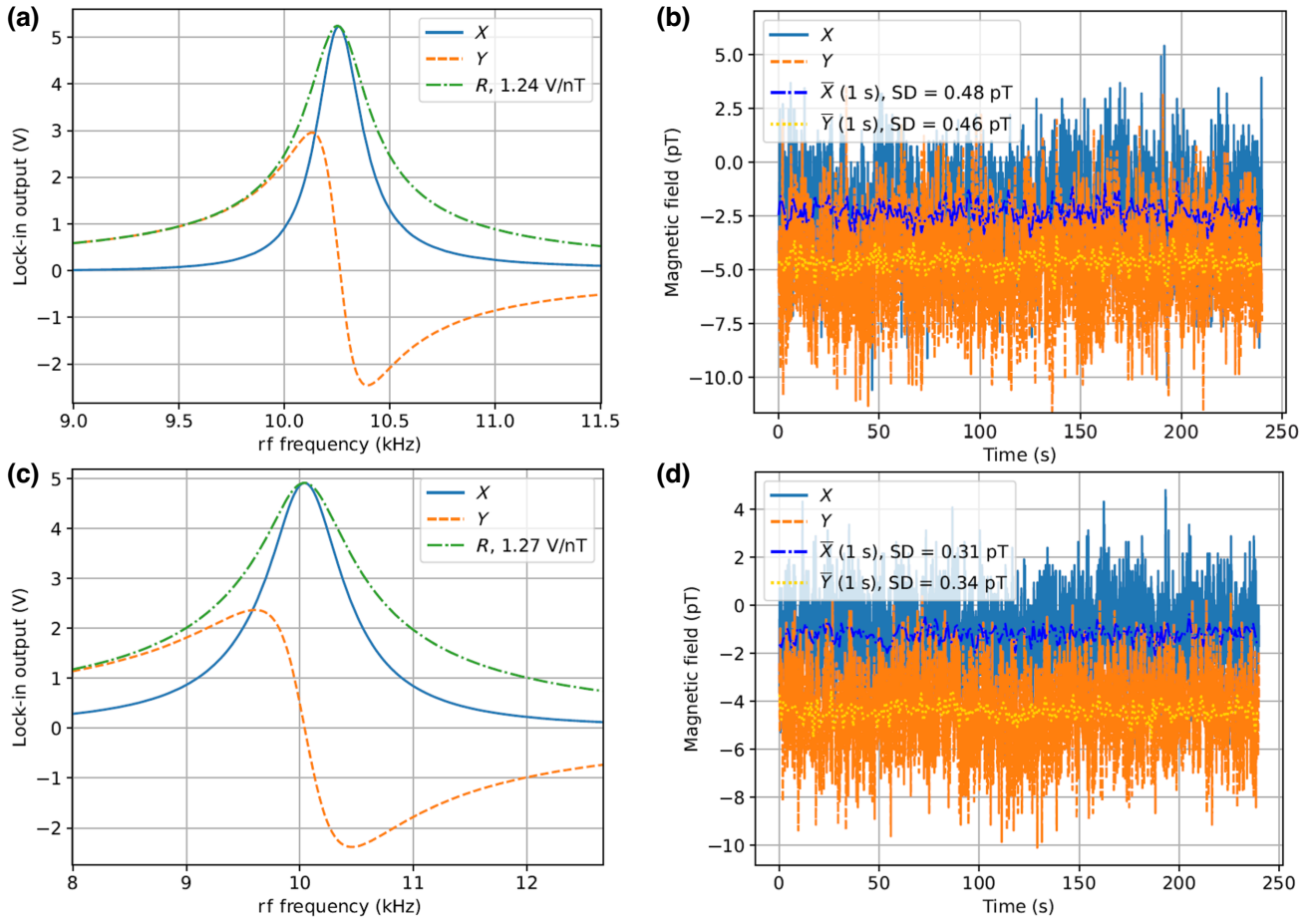
FIG. 5. (a),(b) Sensitivity measurement of the paraffin-coated alignment-based magnetometer ($T \sim 20\,°C$) at a Larmor frequency of $\nu_L = 10.25$ kHz. (a) Magnetic resonance with the rf frequency swept between 9 and 11.5 kHz. (b) A 240 s time trace of the intrinsic OPM noise with the lock-in amplifier demodulating signals at ν_L. Solid and dashed lines labeled X and Y show the raw data sampled at a 10 kHz frequency. Dash-dotted and dotted lines denoted $\bar{X}(1\,s)$ and $\bar{Y}(1\,s)$ show the data when binned and averaged over 1 second segments. (c),(d) Sensitivity measurement of the 65 Torr N_2 ($T \sim 55\,°C$) at a Larmor frequency of $\nu_L = 10.04$ kHz. (c) Magnetic resonance with the rf frequency swept between 8 and 12.5 kHz. (d) A 240 s time trace of the intrinsic OPM noise with the lock-in amplifier demodulating signals at ν_L.

B_{rf}. Once this calibration is completed in Fig. 5(a), the lock-in demodulation frequency is fixed to the Larmor frequency, the rf amplitude is set to zero ($B_{rf} = 0$), and a 4-min time trace of the intrinsic noise of the OPM is taken [see Fig. 5(b)]. Following on from this, the light hitting the balanced photodetector is completely blocked and another time trace is obtained (data not shown). The sensitivity to small oscillating magnetic fields δB_{exp}, i.e., the intrinsic OPM noise, is 480 fT/$\sqrt{Hz}$ for X and 460 fT/$\sqrt{Hz}$ for Y. This is calculated using the methods described in Ref. [33] by taking the standard deviations (SDs) of 240×1 s averaged segments, which are included in the legend of Fig. 5(b). The SDs with the light blocked are only just below at 410 fT/$\sqrt{Hz}$ for X and 380 fT/$\sqrt{Hz}$ for Y, meaning that the intrinsic OPM noise is largely dominated by the electronic noise of the balanced photodetector and also due to a small contribution from the electronic noise of the data-acquisition system.

Fundamental quantum limits to the sensitivity are the spin-projection noise δB_{SPN} and the photon shot noise δB_{PSN}, with the total quantum noise $\delta B_{qu} = \sqrt{\delta B_{SPN}^2 + \delta B_{PSN}^2}$. The spin-projection noise can be theoretically calculated by [23,41]

$$\delta B_{SPN} = \frac{2\hbar}{g_F \mu_B \sqrt{nVT_2}}, \qquad (24)$$

where $g_F = 1/4$ for the $F = 4$ Cs ground state, $n \sim 2.2 \times 10^{16}$ m^{-3} ($T \sim 18.5\,°C$) is the number density of Cs atoms, $T_2 \sim 1/(\pi(230 \text{ Hz})) \sim 1.4$ ms is the transverse relaxation time, and $V = (5 \text{ mm})^3$ is the volume of the whole cell. The spin-projection noise is theoretically calculated to be $\delta B_{SPN} \sim 50$ fT/$\sqrt{Hz}$ using the numbers above. An ideal OPM has $\delta B_{SPN} = \delta B_{PSN}$ [23,46], such that $\delta B_{qu} = \sqrt{2}B_{SPN} \sim 70$ fT/$\sqrt{Hz}$. Apart from the electronic noise, another reason that experimentally δB_{exp} does not reach

70 fT/$\sqrt{\text{Hz}}$ is because many atoms are lost to the $F = 3$ ground state where they cannot be probed [see Fig. 2(a)], in effect decreasing n. The intrinsic OPM sensitivity could be improved by heating the vapour cell [23,32], using a larger vapour cell and using a balanced photodetector with less electronic noise.

V. BUFFER-GAS CELL

We now carry out experiments with a hand-blown cylindrical buffer-gas cell (5 mm length, 5 mm diameter) filled with Cs as well as N_2 buffer gas [see Fig. 3(c)]. The buffer-gas cell is surrounded by a Shapal ceramic cylinder, which is chosen for its high thermal conductivity. The ceramic cylinder is wrapped in a nonmagnetic resistive twisted wire and wrapped with heat insulator aerogel and Kapton tape as shown in Fig. 3(d). The buffer-gas cell can then be heated and kept at an elevated temperature by running current through the twisted wire.

The N_2 buffer-gas pressure is determined using absorption spectroscopy as described by Andalkar [47]. The laser power is kept low for these absorption measurements to avoid any optical pumping effects. An absorption spectrum of the buffer-gas cell is obtained, plotted on top of an absorption spectrum of a pure Cs cell (75 mm length and kept at room temperature) in Fig. 6. The pure cell only contains Cs (and neither contains paraffin or buffer gas) and is used as a frequency reference. The absorption spectrum for the pure cell shows four absorption resonances separated by ground- and excited-state hyperfine splittings (9.2, 1.2 GHz), as expected for Cs D1 spectroscopy. The absorption resonances have a Voigt lineshape, which is a convolution of a Lorentzian and Gaussian lineshape. For the pure cell, the Gaussian Doppler width is much larger than the Lorentzian natural linewidth 4.6 MHz full width at half maximum (FWHM) of the Cs excited state. For a buffer-gas cell, collisions between buffer-gas atoms and Cs atoms lead to Lorentzian pressure broadening as well as frequency shifts of the absorption resonances, as seen in Fig. 6. The pressure broadening is extracted by fitting the $F = 3 \rightarrow F' = 3$ and $F = 3 \rightarrow F' = 4$ absorption resonances to a sum of two Voigt profiles and using their relative hyperfine strengths (1/4 and 3/4, respectively) and then repeating the procedure for $F = 4 \rightarrow F' = 3$ and $F = 4 \rightarrow F' = 4$, with hyperfine strengths of 7/12 and 5/12, respectively. The Doppler width Γ_G is fixed (374 MHz FWHM at 51 °C) and the Lorentzian Γ_L [1.26(0.05) GHz] is fitted, corresponding to a pressure of 65(3) Torr, using the conversion of 19.51 MHz/Torr from [47] for the D1 pressure broadening with N_2. The pressure can also be extracted from the shift $-0.54(0.01)$ GHz in resonance frequencies, which corresponds to a pressure of 65(1) Torr. The uncertainties in the calculated pressures arise from fitting uncertainties.
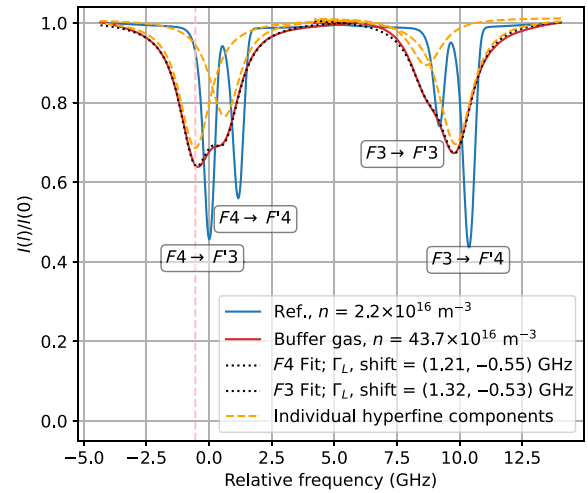

FIG. 6. Absorption spectrum of the D1 line with a 65(3) Torr N_2 cell alongside a frequency reference which is a pure Cs cell. The buffer-gas cell is heated to 51 °C, corresponding to a density of 43.7×10^{16} m^{-3} Cs atoms and a Doppler linewidth $\Gamma_G = 374$ MHz. The $F = 3 \rightarrow F' = 3, 4$ and $F = 4 \rightarrow F' = 3, 4$ transitions are fitted to Voigt profiles and the Lorentzian width Γ_L and pressure shift are extracted.

Our alignment-based magnetometer uses π-polarized light resonant with the $F = 4 \rightarrow F' = 3$ transition [see Fig. 1(b)], as in this case, the $F = 4, m = \pm 4$ states are dark states and atoms become optically pumped into those states with equal probability, creating the spin alignment, as depicted in Fig. 2(b). Note that, for π-polarized light resonant with the $F = 4 \rightarrow F' = 4$ transition, the $F = 4, m = 0$ sublevel will be a dark state instead. With buffer-gas pressure broadening, the $F = 4 \rightarrow F' = 3$ and $F = 4 \rightarrow F' = 4$ resonances begin to overlap. From our fit, we deduce that the overlap is only about 10% for our pressure of 65 Torr N_2 (see Fig. 6 and the thin dotted vertical line). At higher pressures the two transitions will overlap even more. This is problematic for an alignment-based magnetometer as the light in this case will drive both $F = 4 \rightarrow F' = 3$ and $F = 4 \rightarrow F' = 4$ transitions at the same time. The $F = 4, m = \pm 4$ are then not dark states and significantly less spin alignment is created.

To verify whether optical pumping into the $F = 4, m = \pm 4$ states is possible with the 65 Torr N_2 buffer-gas cell where the excited hyperfine states partially overlap (about 10%) and where quenching is the main deexcitation mechanism as described previously, once again the static field is adjusted to be large ($B_0 = 8.38$ G) and a magnetic resonance spectrum is recorded (see Fig. 7). Again, we see the magnetic resonances split due to the nonlinear Zeeman effect, and the two outermost resonances have the largest and equal heights. The frequency difference between the $m = 4 \rightarrow m = 3$ transition and the $m = -3 \rightarrow m = -4$ transition is found experimentally to be $|\Delta \nu_{4,3} - \Delta \nu_{-3,-4}| = 13.2(0.1)$ kHz from a fit of the
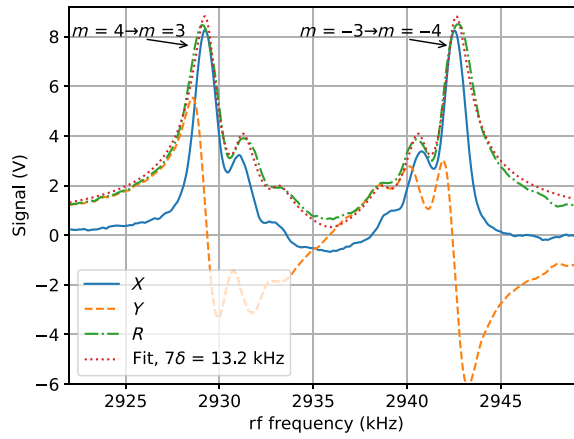
FIG. 7. Nonlinear Zeeman splitting of the magnetic resonances using a 65 Torr N_2 buffer-gas cell heated to about 55 °C. The magnitude R is fitted to Eq. (23). The magnetic resonances for $m = 4 \rightarrow m = 3$ and $m = -3 \rightarrow m = -4$ are indicated.

data in Fig. 7 to Eq. (23), which agrees well with the value $7\delta = 13.1$ kHz calculated from Eqs. (21) and (22).

This experimentally demonstrates that it is possible to generate a spin-aligned stated in the 65 Torr N_2 buffer-gas cell by optically pumping more Cs atoms into the $m = \pm 4$ states than the other magnetic sublevels in the $F = 4$ ground state. It is expected that better optical pumping into the $m = \pm 4$ states will be achieved if a smaller buffer-gas pressure is used, as there will be less unwanted pumping to the $F = 4 \rightarrow F' = 4$ transition. A higher ratio R_p / Γ_1 [see Eq. (19)] will also increase pumping into the $m = \pm 4$ states. The drawback of a lower buffer-gas pressure, however, is that the atoms will diffuse more quickly to the walls, leading to a smaller T_2 time and hence a less sensitive OPM. These two processes compete and need to be taken into consideration when selecting the optimal buffer-gas pressure for an alignment-based magnetometer.

We now characterize the magnetic field sensitivity of the buffer-gas cell using the same procedure as for the paraffin-coated cell. The optimal light power is found to be 30 μW. A magnetic resonance signal at 10 kHz is obtained with the 65 N_2 Torr cell in Fig. 5(c). A 240 s time trace with the rf field turned off is shown in Fig. 5(d). The sensitivity of the OPM, defined as the SD of the 240×1 s data points in Fig. 5(d), is 310 fT/$\sqrt{\text{Hz}}$ for X and 340 fT/$\sqrt{\text{Hz}}$ for Y, with the average of the quadratures being 325 fT/$\sqrt{\text{Hz}}$. The electronic noise is 190 fT/$\sqrt{\text{Hz}}$, which means that it is no longer the dominant noise source, unlike in the case of the paraffin-coated cell. This is because higher optical powers are used for the buffer-gas cell. The sensitivity of the buffer-gas cell therefore exceeds the paraffin-coated cell in this paper. The sensitivity is mainly limited by laser shot noise and electronic noise of the balanced photodetector.

We use Eq. (24) to calculate the predicted quantum limited spin-projection noise. The number density $n =$

60×10^{16} m^{-3} at $T = 55$ °C and $T_2 = 1/(\pi(800$ Hz$))$. In a buffer-gas cell only the atoms inside the beam are probed, unlike in a paraffin-coated cell where all the atoms in the cell are probed. We therefore use the volume inside the beam $V = V_{\text{beam}} = 3.9 \times 10^{-9}$ m^3, where the diameter of the beam is about 1 mm and the length of the cell is 5 mm. Inserting the numbers above, we estimate the atomic noise to be $\delta B_{\text{SPN}} \sim 100$ fT/$\sqrt{\text{Hz}}$. An ideal OPM [46] would therefore have a quantum limited sensitivity of $\delta B_{\text{qu}} = \sqrt{2}\delta B_{\text{SPN}} \sim 140$ fT/$\sqrt{\text{Hz}}$, less than a factor of 3 different to the intrinsic OPM noise measured here. As described earlier, one reason why the experimentally measured quantum noise is higher than theoretically predicted is because many of the atoms are lost to the $F = 3$ ground state [see Fig. 2(b)], where they are not probed. A better sensitivity could be obtained by further heating the vapour cell to increase the density of atoms or by increasing the diameter and length of the cell, whilst increasing the size of the beam. If a 5 mm diameter beam is used, probing the whole cell, the atomic noise is estimated to be $\delta B_{\text{SPN}} \sim 20$ fT/$\sqrt{\text{Hz}}$. Multipass [8] and cavity-enhanced [48] schemes could also be implemented, which would enhance the sensitivity. Note that many atoms are lost to the $F = 3$ ground state (see Fig. 2), reducing the number of Cs atoms that are probed. Using a second laser beam (typically called a repumper) bringing the atoms out of $F = 3$ and back into $F = 4$ would also increase the number of probed atoms, improving the sensitivity of the rf OPM.

VI. CONCLUSIONS

The results presented in this paper demonstrate the first implementation of a one-beam rf OPM, the alignment-based magnetometer, being used with a buffer-gas cell. The sensitivity of the alignment-based magnetometer with Cs alkali vapour and 65 Torr N_2 buffer gas is 325 fT/$\sqrt{\text{Hz}}$. This sensitivity could be further improved upon by using a larger-diameter laser beam. The optical powers used are ≤ 30 μW, importantly meaning that low-cost vertical cavity surface-emitting laser (VCSEL) diodes could be used as a light source in portable sensors. Further studies could investigate the optimal vapour cell size, operating temperature, and buffer-gas pressure. Although our experiments are carried out using hand-blown vapour cells, we expect similar performance with microfabricated buffer-gas cells. Our work opens up the possibility of the commercialization of compact, robust, and portable rf OPMs using only one low-power laser beam with buffer-gas cells, a much more scalable and commercially viable option than using paraffin-coated vapour cells. In the future miniaturized, low-power, and highly sensitive alignment-based rf OPMs could be a promising alternative to traditional fluxgate magnetometers (e.g., Bartington MAG639 [49]) and induction coils (e.g., MEDA MGCH-2 [50]) for detecting oscillating and rf magnetic fields. We also note that the

more recent OPMs based on nitrogen-vacancy centers in diamond [51–53] can achieve high sensitivity.

Further data are available from the authors upon request.

ACKNOWLEDGMENTS

[1] E. Labyt, T. Sander-Thömmes, and R. Wakai, *Flexible High Performance Magnetic Field Sensors: On-Scalp Magnetoencephalography and Other Applications* (Springer, Cham, 2022).

[2] M. Auzinsh, D. Budker, and S. M. Rochester, *Optically Polarized Atoms: Understanding Light-Atom Interactions* (Oxford University Press, Oxford, 2014).

[3] D. Budker and M. Romalis, Optical magnetometry, Nat. Phys. **3,** 227 (2007).

[4] F. Beato, E. Belorizky, E. Labyt, M. Le Prado, and A. Palacios-Laloy, Theory of a ^{4}He parametric-resonance magnetometer based on atomic alignment, Phys. Rev. A **98,** 053431 (2018).

[5] I. K. Kominis, T. W. Kornack, J. C. Allred, and M. V. Romalis, A subfemtotesla multichannel atomic magnetometer, Nature **422,** 596 (2003).

[6] W. Wasilewski, K. Jensen, H. Krauter, J. J. Renema, M. V. Balabas, and E. S. Polzik, Quantum Noise Limited and Entanglement-Assisted Magnetometry, Phys. Rev. Lett. **104,** 133601 (2010).

[7] W. Chalupczak, R. M. Godun, S. Pustelny, and W. Gawlik, Room temperature femtotesla radio-frequency atomic magnetometer, Appl. Phys. Lett. **100,** 242401 (2012).

[8] H. Yao, B. Maddox, and F. Renzoni, High-sensitivity operation of an unshielded single cell radio-frequency atomic magnetometer, Opt. Express **30,** 42015 (2022).

[9] D. A. Keder, D. W. Prescott, A. W. Conovaloff, and K. L. Sauer, An unshielded radio-frequency atomic magnetometer with sub-femtotesla sensitivity, AIP Adv. **4,** 127159 (2014).

[10] Quspin. https://quspin.com, (December 2022).

[11] Fieldline inc. https://fieldlineinc.com/, (December 2022).

[12] Twinleaf. https://twinleaf.com/, (December 2022).

[13] I. M. Savukov, S. J. Seltzer, M. V. Romalis, and K. L. Sauer, Tunable Atomic Magnetometer for Detection of Radio-Frequency Magnetic Fields, Phys. Rev. Lett. **95,** 063004 (2005).

[14] I. M. Savukov and M. V. Romalis, NMR Detection with an Atomic Magnetometer, Phys. Rev. Lett. **94,** 123001 (2005).

[15] S. K. Lee, K. L. Sauer, S. J. Seltzer, O. Alem, and M. V. Romalis, Subfemtotesla radio-frequency atomic magnetometer for detection of nuclear quadrupole resonance, Appl. Phys. Lett. **89,** 214106 (2006).

[16] R. J. Cooper, D. W. Prescott, P. Matz, K. L. Sauer, N. Dural, M. V. Romalis, E. L. Foley, T. W. Kornack, M. Monti, and J. Okamitsu, Atomic magnetometer multisensor array for RF interference mitigation and unshielded detection of nuclear quadrupole resonance, AIP Adv. **6,** 064014 (2016).

[17] S. M. Rochester, PhD Thesis, UC Berkeley, 2010.

[18] C. Deans, L. Marmugi, and F. Renzoni, Sub-picotesla widely tunable atomic magnetometer operating at room-temperature in unshielded environments, Rev. Sci. Instrum. **89,** 083111 (2018).

[19] C. Deans, Y. Cohen, H. Yao, B. Maddox, A. Vigilante, and F. Renzoni, Electromagnetic induction imaging with a scanning radio frequency atomic magnetometer, Appl. Phys. Lett. **119,** 014001 (2021).

[20] J. E. Dhombridge, N. R. Claussen, J. Iivanainen, and P. D. D. Schwindt, High-Sensitivity rf Detection Using an Optically Pumped Comagnetometer Based on Natural-Abundance Rubidium with Active Ambient-Field Cancellation, Phys. Rev. Appl. **18,** 044052 (2022).

[21] P. Bevington and W. Chalupczak, Different configurations of radio-frequency atomic magnetometers–A comparative study, Sensors **22,** 9741 (2022).

[22] B. Maddox and F. Renzoni, Two-photon electromagnetic induction imaging with an atomic magnetometer, Appl. Phys. Lett. **122,** 144001 (2023).

[23] M. P. Ledbetter, V. M. Acosta, S. M. Rochester, D. Budker, S. Pustelny, and V. V. Yashchuk, Detection of radio-frequency magnetic fields using nonlinear magneto-optical rotation, Phys. Rev. A **75,** 023405 (2007).

[24] T. Zigdon, A. D. Wilson-Gordon, S. Guttikonda, E. J. Bahr, O. Neitzke, S. M. Rochester, and D. Budker, Nonlinear magneto-optical rotation in the presence of a radio-frequency field, Opt. Express **18,** 25494 (2010).

[25] S. M. Rochester, Nonlinear magneto-optical rotation in a radio-frequency field. http://rochesterscientific.com/, (December 2022).

[26] A. Weis, G. Bison, and A. Pazgalev, Theory of double resonance magnetometers based on atomic alignment, Phys. Rev. A **74,** 033401 (2006).

[27] S. J. Ingleby, C. O'Dwyer, P. F. Griffin, A. S. Arnold, and E. Riis, Vector Magnetometry Exploiting Phase-Geometry Effects in a Double-Resonance Alignment Magnetometer, Phys. Rev. Appl. **10,** 034035 (2018).

[28] M. V. Balabas, T. Karaulanov, M. P. Ledbetter, and D. Budker, Polarized Alkali-Metal Vapor with Minute-Long Transverse Spin-Relaxation Time, Phys. Rev. Lett. **105,** 070801 (2010).

[29] W. Li, M. Balabas, X. Peng, S. Pustelny, A. Wickenbrock, H. Guo, and D. Budker, Characterization of high-temperature performance of cesium vapor cells with anti-relaxation coating, J. Appl. Phys. **121,** 063104 (2017).

[30] V. Shah, S. Knappe, P. D. D. Schwindt, and J. Kitching, Subpicotesla atomic magnetometry with a microfabricated vapour cell, Nat. Photonics **1,** 649 (2007).

[31] S. Dyer, P. F. Griffin, A. S. Arnold, F. Mirando, D. P. Burt, E. Riis, and J. P. McGilligan, Micro-machined deep silicon atomic vapor cells, J. Appl. Phys. **132,** 134401 (2022).

[32] S. Seltzer, PhD Thesis, Princeton University, 2008.

[33] L. M. Rushton, T. Pyragius, A. Meraki, L. Elson, and K. Jensen, Unshielded portable optically pumped magnetometer for the remote detection of conductive objects using eddy current measurements, Rev. Sci. Instrum. **93**, 125103 (2022).

[34] C. Deans, L. Marmugi, and F. Renzoni, Sub-Sm-1 electromagnetic induction imaging with an unshielded atomic magnetometer, Appl. Phys. Lett. **116**, 133501 (2020).

[35] K. Jensen, M. Zugenmaier, J. Arnbak, H. Stærkind, M. V. Balabas, and E. S. Polzik, Detection of low-conductivity objects using eddy current measurements with an optical magnetometer, Phys. Res. **1**, 033087 (2019).

[36] L. Marmugi and F. Renzoni, Optical magnetic induction tomography of the heart, Sci. Rep. **6**, 23962 (2016).

[37] C. Deans, L. Marmugi, and F. Renzoni, Active underwater detection with an array of atomic magnetometers, Appl. Optics **57**, 2346 (2018).

[38] P. Bevington, R. Gartman, and W. Chalupczak, Object detection with an alkali-metal spin maser, J. Appl. Phys. **130**, 214501 (2021).

[39] P. Bevington, R. Gartman, and W. Chalupczak, Enhanced material defect imaging with a radio-frequency atomic magnetometer, J. Appl. Phys. **125**, 094503 (2019).

[40] D. A. Steck, Cs D line data. https://steck.us/alkalidata/cesiumnumbers.1.6.pdf, (December 2022).

[41] M. T. Graf, D. F. Kimball, S. M. Rochester, K. Kerner, C. Wong, D. Budker, E. B. Alexandrov, M. V. Balabas, and V. V. Yashchuk, Relaxation of atomic polarization in paraffin-coated cesium vapor cells, Phys. Rev. A **72**, 023401 (2005).

[42] S. Eckel, D. Barker, E. Norrgard, and J. Scherschligt, Pylcp: A python package for computing laser cooling physics, (to be published 2020).

[43] B. Julsgaard, PhD Thesis, University of Aarhus, 2003.

[44] S. J. Seltzer and M. V. Romalis, High-temperature alkali vapor cells with antirelaxation surface coatings, J. Appl. Phys. **106**, 114905 (2009).

[45] G. Bao, A. Wickenbrock, S. Rochester, W. Zhang, and D. Budker, Suppression of the Nonlinear Zeeman Effect and Heading Error in Earth-Field-Range Alkali-Vapor Magnetometers, Phys. Rev. Lett. **120**, 033202 (2018).

[46] M. Auzinsh, D. Budker, D. F. Kimball, S. M. Rochester, J. E. Stalnaker, A. O. Sushkov, and V. V. Yashchuk, Can a Quantum Nondemolition Measurement Improve the Sensitivity of an Atomic Magnetometer?, Phys. Rev. Lett. **93**, 173002 (2004).

[47] A. Andalkar and R. B. Warrington, High-resolution measurement of the Pressure broadening and shift of the Cs D1 and D2 lines by N_2 and He buffer gases, Phys. Rev. A **65**, 032708 (2002).

[48] H. Crepaz, L. Y. Ley, and R. Dumke, Cavity enhanced atomic magnetometry, Sci. Rep. **5**, 15448 (2015).

[49] Bartington Mag639 wide bandwidth https://www.bartington.com/products/high-performance-magnetometers/mag639-wide-bandwidth/, (April 2023).

[50] MEDA MGCH-2 Single Axis AC Magnetic Field Sensor http://www.meda.com/index.php/products?name=MGCH-2, (April 2023).

[51] J. M. Taylor, P. Cappellaro, L. Childress, L. Jiang, D. Budker, P. R. Hemmer, A. Yacoby, R. Walsworth, and M. D. Lukin, High-sensitivity diamond magnetometer with nanoscale resolution, Nat. Phys. **4**, 810 (2008).

[52] T. Wolf, P. Neumann, K. Nakamura, H. Sumiya, T. Ohshima, J. Isoya, and J. Wrachtrup, Subpicotesla Diamond Magnetometry, Phys. Rev. X **5**, 041001 (2015).

[53] Y. Silani, J. Smits, I. Fescenko, M. W. Malone, A. F. McDowell, A. Jarmola, P. Kehayias, B. Richards, N. Mosavian, N. Ristoff, and V. M. Acosta, Nuclear quadrupole resonance spectroscopy with a femtotesla diamond magnetometer, arxiv:2302.12401 (2023).